Nanoscale

ROYAL SOCIETY OF CHEMISTRY

PAPER

View Article Online
View Journal | View Issue

Cite this: *Nanoscale*, 2023, **15**, 6745

pH/ROS-responsive propelled nanomotors for the active treatment of renal injury†

Fei Tong, *‡[a,b,c,d] Jin Liu,‡[e] Lei Luo,‡[f] Lingyan Qiao,‡[g] Jianming Wu, [a,b] Guosheng Wu*[c] and Qibing Mei*[a,b]

Received 5th January 2023,
Accepted 4th March 2023

DOI: 10.1039/d3nr00062a

rsc.li/nanoscale

Effective drugs that can be quickly delivered to and retained for a long time in the renal tubule are necessary for acute kidney injury (AKI) treatment. In this study, a gold nanoparticle-modified mesoporous silica (Au@MSN-NH_2)-camouflaged (methoxyphenyl)(morpholino)phosphinodithioic acid (GYY4137) asymmetrical nanosystem decorated with L-serine (S; an AKI-targeting agent) and D-Arg-dimethylTyr-Lys-Phe-NH_2 (TK-SS31; a reactive oxygen species (ROS)-sensitive thioketal linker/mitochondria-targeted antioxidant) was constructed for the treatment of renal tubule and mitochondrial injury as well as the synergistic and active treatment of AKI. Due to the enhanced permeability and retention (EPR) of nanomotors, they could progressively accumulate in renal sites. The asymmetrical nanosystem achieved effective drug distribution in the kidney as well as pH-responsive hydrogen sulfide (H_2S) release and ROS-responsive SS31 release, resulting in an active therapeutic effect mediated by nanomotor motion resulting from asymmetrical H_2S release.

A cute kidney injury (AKI), which is characterized by a rapid decline in renal function, has a variety of etiologies, and is associated with increased morbidity and mortality.[1] AKI can occur in patients without previous renal disease or those with chronic kidney disease (1). AKI mainly results from the use of toxic drugs, renal ischemia/reperfusion injury (RI/RI), and concomitant chronic diseases.[2–6] Although progress has been made in the development of clinical strategies, AKI still requires surgical treatment, and mortality remains high in the hospital.[6–9] Consequently, an effective pharmacological treatment method for AKI is urgently needed.

Oxidative stress is considered a vital mechanism in the complicated pathogenesis of AKI.[10–13] Previous studies have revealed that reactive oxygen species (ROS) are associated with AKI and activate cascades in the mitochondria (the primary source of ROS) to induce renal injury.[11,14–20] D-Arg-dimethylTyr-Lys-Phe-NH_2 (SS31) has been found to be a mitochondria-targeted antioxidant and to clear ROS in the context of AKI.[11,21–25] Previous studies have shown that SS31 can selectively bind cardiolipin and protect mitochondrial cristae from AKI-induced damage.[11,26] It has been reported that (methoxyphenyl)(morpholino)phosphinodithioic acid (GYY4137) can release hydrogen sulfide (H_2S) and alleviate AKI.[27–29] In particular, GYY4137 slowly releases relatively low levels of H_2S under physiological conditions.[27–29] Nevertheless, H_2S release from GYY4137 is increased under acidic conditions. In previous studies, GYY4137 or SS31 was loaded into nanomaterials to maintain H_2S or SS31 contents *in vitro*/*in vivo*.[29,30]

With the rapid advancement of nanotechnology, issues related to drug delivery in the treatment of AKI have been effectively solved.[30] In particular, researchers have recently performed *in vitro*/*vivo* studies on micro/nanomotors.[31,32] These studies have revealed that micro/nanomotors can be readily propelled in different environments and exert better effects than their static counterparts *in vitro*/*vivo*.[33] Based on the immense research progress on the use of micro/nanomotors, we developed a pH/ROS-sensitive L-serine (*S*)-decorated micro/nanomotor that can improve the delivery of H_2S/SS-31 for the treatment of AKI.

[a]*Education Ministry Key Laboratory of Medical Electrophysiology, Sichuan Key Medical Laboratory of New Drug Discovery and Druggability Evaluation, Luzhou, China*

[b]*Key Laboratory of Activity Screening and Druggability Evaluation for Chinese Materia Medica, School of Pharmacy, Southwest Medical University, Luzhou, 646000, China. E-mail: qbmei53@hotmail.com, tongxuchang@163.com, jianmingwu@swmu.edu.cn*

[c]*School of Medicine, Zhejiang University, Hangzhou 310003, Zhejiang Province, China. E-mail: guosheng_wu@zju.edu.cn*

[d]*Department of Pharmacology, School of Pharmacy, Binzhou Medical University, Yantai, 264003, PR China*

[e]*Key Laboratory of Tropical Biological Resources of Ministry of Education and One Health Institute, School of Pharmaceutical Sciences, Hainan University, Haikou 570228, China. E-mail: liujin9108@163.com*

[f]*Institute of Molecular Medicine (IMM), Renji Hospital, School of Medicine, Shanghai Jiao Tong University, Shanghai 200240, China. E-mail: 15917917574@163.com*

[g]*The First Clinical medical College, Binzhou Medical University, Yantai, 264003, PR China. E-mail: joann_1029@163.com*

†Electronic supplementary information (ESI) available. See DOI: https://doi.org/10.1039/d3nr00062a

‡These authors contributed equally to this work.

The pH/ROS-activated nanomotors were synthesized by modifying the surface of GYY4137-loaded mesoporous silica nanoparticles (NH_2-MSNs) with the kidney tubule-targeting moiety "S" and the thioketal linker D-Arg-dimethylTyr-Lys-Phe-NH_2 (TK-SS31) on one side and further attaching Au to the opposite side (the nanomotors are hereafter referred to as Au@SS31-TK-MSN/GYY4137@S (ASMGS) nanomotors, Scheme 1). Then, the nanomotor accumulates in the kidney tubule due to the high affinity of "S" for kidney injury molecule-1 (Kim-1), resulting in the fast release of H_2S from the prodrug GYY4137 into the low-pH environment of lysosomes. By virtue of the asymmetrical nature of nanomotors, the asymmetrical release of H_2S propels the nanomotors. Meanwhile, TK-SS31 is also detached, leading to asymmetrical SS31 release in the mitochondria, in which there are high ROS levels. To the best of our knowledge, these pH-activated nanomotors, which have motor ability and can asymmetrically release and actively deliver H_2S, are the first nanomotors used for the treatment of AKI *in vivo*. Out findings may not only expand the biomedical applications of micro/nanomotors but also provide novel theoretical evidence and a foundation for the study of treatments for renal damage.

Methods

Materials

GYY4137 was purchased from Shanghai Maokang Biotechnology Co., Ltd (China). SS31 was purchased from Nanjing Peptide Industry Biotechnology Co., Ltd (China). L-Serine antibodies were obtained from Shenzhen Wenle Biotechnology Co., Ltd (China). All antibodies were obtained from Guangzhou Baihui Biotechnology Co., Ltd (China). Other organic solvents and reagents were obtained from Southern Medical University, Binzhou Medical University and Southwest Medical University (China).

Synthesis of nanoparticles

Aminized mesoporous silica (MSN-NH_2) was dissolved in PBS by ultrasonic dispersion. After that, an appropriate amount of GYY4137 (in DMSO) was mixed into the system and the mixed solution was centrifuged and washed twice, followed by further attachment of the gold nanoparticles on the opposite side by sputter coater. Using an EDC-NHS reaction, we introduced L-serine into the MSN plugging opposite surface to obtain a Au@MSN/GYY4137@S solution. Next, the SS31-TK solution was added, followed by EDS and NHS to activate carboxyl. Ultimately, Au@SS31-TK-MSN/GYY4137@S was successfully obtained.

Characterization

The morphology of ASMGS was studied *via* transmission electron microscopic (TEM) images (JEM, 120 kV, Japan). In addition, the size of the ASMGS was observed using a Zetasizer Nano (Marvin Instruments Co. Ltd, England).

H_2S level and release measurement

Briefly, 5 mL ASMGS was added into a dialysis bag and immersed in 80 mL of different pH buffers and H_2O_2 at 37 °C. At fixed time points, H_2S concentrations were examined using a H_2S kit, and the solution was replenished with an equivo-

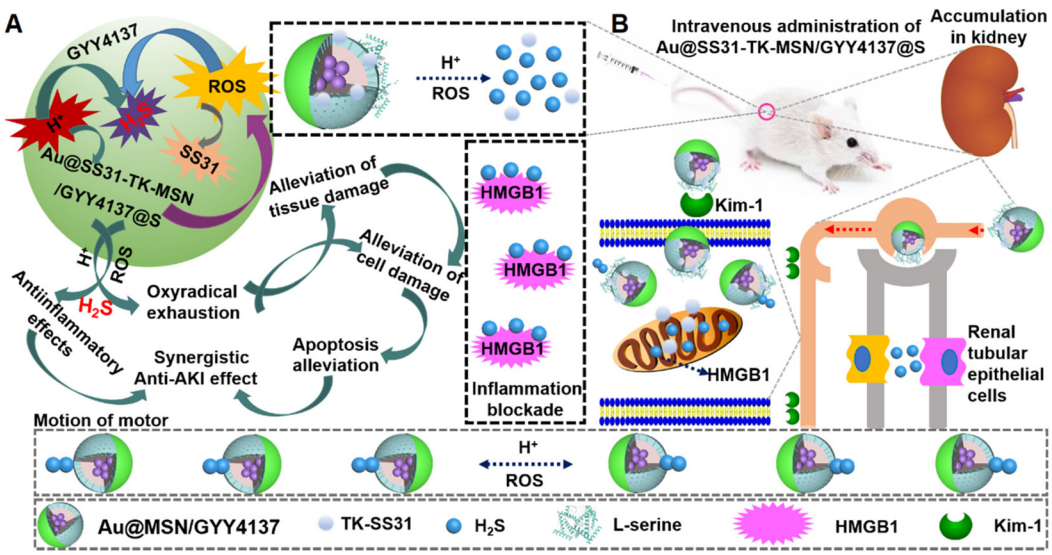

Scheme 1 Schematic illustration of Au@SS31-TK-MSN/GYY4137@S (ASMGS) nanomotors, which can achieve active delivery of H_2S and SS31 to alleviate AKI. (A) Structure of ASMGS nanomotors. The prodrug GYY4137 was first loaded into NH_2-MSNs, and the kidney tubule-targeting moiety "S" and TK-SS31 were then attached to one side. Then, Au was attached to the surface on the opposite side. (B) Effect of ASMGS nanomotors in alleviating AKI. In the low-pH environment of lysosomes, they result in fast release of H_2S from the prodrug GYY4137, and in the mitochondria, in which ROS levels are high, TK-SS31 is detached, leading to rapid SS31 release. The release of H_2S propels the nanomotor, further improving the therapeutic effect on AKI.

luminal volume of fresh buffer. Then, the percentage of H_2S release was calculated.

SS31 release

Briefly, 5 mL ASMGS was added to a dialysis bag and immersed in 80 mL of 10 mM H_2O_2 at 37 °C. At fixed time points, SS31 levels were measured by HPLC, and the solution was replenished with an equivoluminal volume of fresh buffer. Then, the percentage of SS31 release was calculated.

Cell viability

The *in vitro* cytotoxicity was estimated by the CCK-8 assay. Briefly, HKC cells (5×10^6) were incubated in 96-well cell culture plates at room temperature overnight. Fresh DMEM containing different concentrations of ASMGS was added and cultured for 24 h. In addition, the culture media were replaced with fresh DMEM including ASMGS (300 μg mL^{-1}) and cultured for 24 h. The CCK-8 solution (100 μL) was added for 2 h after washing twice with PBS. Then, the absorbance was inspected at 450 nm to obtain the cell survival rates.

In vitro AKI model

Logarithmic HKC cells were seeded into 96-well plates (200 μL per well) and cultured for 24 h. Cells were washed three times with phosphate buffer (PBS) and replaced with a sugar-free Krebs solution. Then, $Na_2S_2O_4$ (2 mmol L^{-1}) was added to the Krebs solution and the culture dish was placed in a sealed anaerobic gas-producing bag, to which 95% N_2/5% CO_2 was added and incubated at 37 °C for 40 min. The HKC cells were replaced (MEM medium containing 10% Gibco FBS) and incubated in an incubator (air + 5% CO_2, 37 °C) for a further 24 h.

Kim-1-associated endocytosis of ASMGS

AKI model cells were seeded into 96-well plates (200 μL per well). A culture medium containing Cy5-conjugated ASMGS (60 μmol L^{-1}) was added into the 96-well plates (200 μL per well) and cultured for 6 h. Next, the HKC cells were washed twice with a serum-free medium and observed by CLSM.

AKI model cells were seeded into 96-well plates (200 μL per per well). A culture medium containing FITC-kim-1 antibodies was added into the 96-well plates (200 μL per well) and cultured for 12 h. Then, ASMGS (60 μmol L^{-1}) was added and incubation was continued. Next, the HKC cells were washed twice with a serum-free medium and observed by CLSM.

ROS-triggered disruption of ASMGS and mitochondrial transmembrane potential

AKI model cells were seeded into 96-well plates (200 μL per well). A culture medium containing AF488-conjugated ASMGS (60 μmol L^{-1}) was added into the 96-well plates (200 μL per well) and cultured for 6 h. Next, the HKC cells were washed twice with a serum-free medium and observed by CLSM.

AKI model cells were seeded into 96-well plates (200 μL per well). A culture medium containing ASMGS (60 μmol L^{-1}) was added into the 96-well plates (200 μL per well) and cultured for 6 h. Then, the mitochondrial red probe was added and cultured for 30 min. Next, the HKC cells were washed twice with a serum-free medium and observed by CLSM.

In vitro ROS evaluation

AKI model cells were seeded into 96-well plates (200 μL per well). A culture medium containing ASMGS (60 μg mL^{-1}) was added into the 96-well plates (200 μL per well) and cultured for 6 h. Then, DCFH-DA was added and cultured for 30 min. Next, the HKC cells were washed twice with a serum-free medium and observed by CLSM.

In vitro LAMP1, caspase-3, HMGB1 and CRT expressions

AKI model cells were seeded into 96-well plates (200 μL per well). A culture medium containing AF488-LAMP1, Cy3-caspase-3, AF488-HMGB1 and AF488-CRT antibodies was added into the 96-well plates (200 μL per well) and cultured for 12 h, respectively. Then, ASMGS (60 μmol L^{-1}) was added and incubation was continued. Next, the HKC cells were washed twice with a serum-free medium and observed by CLSM.

In vitro cell pyroptosis

AKI model cells were seeded into 96-well plates (200 μL per well). A culture medium containing AF594-GSDMD, AF594-caspase-11 and AF488-IL-18 antibodies was added into the 96-well plates (200 μL per well) and cultured for 12 h, respectively. Then, ASMGS (60 μmol L^{-1}) was added and incubation was continued. Next, the HKC cells were washed twice with a serum-free medium and observed by CLSM.

AKI model cells were seeded into 96-well plates (200 μL per well). A culture medium containing ASMGS (60 μmol L^{-1}) was added into the 96-well plates (200 μL per well) and cultured for 6 h. Then, the HKC cells were washed twice with a serum-free medium and observed by TEM.

Optical video recording

The motion of the ASMGS motors was observed using an inverted fluorescence microscope. First, the diluted ASMGS motor solution was placed on a hydrophilic glass slide in different media. To observe the H_2S release movement from the ASMGS motor, videos were recorded using a camera. The velocity and diffusion coefficient of the ASMGS motors were observed using ImageJ and Chemotaxis. The *MSD* was estimated and calculated using $MSD = 4D\Delta t + V^2\Delta t^2$, where D is the diffusion coefficient of Brownian motion and V the velocity of autonomous motion.

Animal and AKI models

All animal experimentation procedures were consistent with the guidelines of the Institutional Animal Care and Use Committee of Southwest Medical University. All the experiments complied with the relevant laws or guidelines. All of the experiments followed the institutional guidelines. All animal procedures were performed in accordance with the Guide for the Care and Use of Laboratory Animals of "Southwest Medical University", and the experiments were approved by the Animal Ethics Committee of "Southwest Medical University". BALB/c

mice were acquired and kept at the Laboratory Animal Center of Southwest Medical University. The mice were anaesthetized with pentobarbital sodium (35 mg kg^{-1}) and the cavum abdominis was opened to separate the renal artery and vein of the left kidney. In addition, the renal artery and vein were blocked for 45 min and reperfusion was performed for 48 hours.

In vivo fluorescence, magnetic resonance (MR)/X-ray/ brightness-mode ultrasound imaging

After intravenous injection of ASMGS motors (5 mg kg^{-1}), the *in vivo* fluorescence distribution in the AKI mouse was observed at fixed times using a multimode small-animal imaging system *in vivo* (FX Pro; Bruker, USA).

Subsequently, the renal injury region in the mice was observed using a small-animal MR/X-ray imaging system (Bruker Biospin MRI GmbH). Then, the renal blood flow was measured by MR/brightness-mode ultrasound imaging. Furthermore, a dynamic *in vivo* MR imaging video was observed.

Pharmacological effects of asymmetrical PSMGS *in vivo*

Following intravenous injection of ASMGS motors (5 mg kg^{-1}), the serum and tissues (kidney, heart, liver and lung) were separated after 48 h reperfusion. The BUN, Scr, HE staining, TUNEL staining and immunochemistry were measured.

Statistical analysis

The statistical significance of differences in data for the therapeutic groups was assessed by one-way ANOVA with a *post hoc* test. The values of $P < 0.01$ were considered to indicate statistical significance in all analyses.

Results

Fabrication and characterization of Au@SS31-TK-MSN/ GYY4137@S (ASMGS) nanomotors

As shown in Fig. 1A, the prodrug GYY4137 was incubated with NH_2-MSNs (synthesized over 24 h as described in our previous study to achieve successful prodrug loading).[34] After dialysis to eliminate free GYY4137, the percentage of prodrug that was successfully loaded on Au@MSNs was ~7.8%, which is consistent with a previous report (ESI Fig. S1†).[29] The kidney tubule-targeting moiety "S" was attached to one side of Au@MSNs, with a grafting percentage of 11.4% (ESI Fig. S1†), and then the thioketal linker TK-SS31 was attached to the surface, with grafting percentages of 5.6%, respectively (ESI Fig. S1–3†). The amount of H_2S released from GYY4137 in PBS (pH, 7.4) + HCl and PBS (pH, 7.4) was determined. As shown in Fig. 1B, the H_2S content quickly increased in PBS (pH, 7.4) + HCl (0.1 mol L^{-1}), whereas the H_2S content slowly increased in PBS (pH, 7.4), indicating that H_2S release from GYY4137 was pH-sensitive. Subsequently, the amount of H_2S released from ASMGS nanomotors under acidic conditions and in the presence of H_2O_2 was assessed, and the results are shown in Fig. 1C–G. H_2S was released over 72 h in the presence of 10 mM H_2O_2, in an environment of pH 5.0 and in an environment of pH 5.0 containing 10 mM H_2O_2, indicating long-term pH/ROS-triggered H_2S release from the formed ASMGS nanomotors.

After successful synthesis, the samples were subsequently characterized by TEM and mapping (Fig. 2), and it was determined from the TEM images that the average size of the spherical structure was determined to be 73 nm. Next, the stability and particle size change of the samples were observed, and the results are shown in ESI Fig. S4 and 5.† In addition, the SEM, AFM, FT-IR spectroscopy, CD and XPS were also performed to study the stabilization of nanomotors (ESI Fig. S6†). The results indicated that ASMGS nanomotors possessed a stable structure.

In vitro evaluation of ASMGS nanomotors

After ASMGS nanomotors were prepared and characterized, the amount of H_2S released from ASMGS nanomotors in an *in vitro* AKI model was assessed, and the results are shown in ESI Fig. S7.† Subsequently, HKC cells (proximal tubular epithelial cells) were utilized to evaluate the cytotoxicity of ASMGS nanomotors. As shown in ESI Fig. S8,† cell viability was high even when the concentration of ASMGS nanomotors was 300 μg mL^{-1}, indicating that the nanocarrier had good stability and low toxicity.

Kim-1 is a transmembrane glycoprotein in renal tubular epithelial cells and a member of immunoglobulin gene superfamily. The expression of kim-1 is significantly upregulated in AKI.[35] In addition, "S", as a renal tubule–targeted modifier, can target kim-1 in the context of AKI.[30,36] In our study, a greater uptake of Cy5-conjugated ASMGS nanomotors by AKI model HKC cells was associated with the interaction between kim-1 and Cy5-conjugated ASMGS nanomotors (Fig. 3A). However, CLSM corroborated that kim-1 expression was obviously increased in the *in vitro* AKI model (Fig. 3B). In addition, kim-1 expression was significantly decreased in the presence of ASMGS nanomotors in the *in vitro* AKI model (Fig. 3B), implying that ASMGS nanomotors decreased kim-1 expression by releasing H_2S and SS31. These results illustrated that ASMGS nanomotors could target kim-1, which is associated with AKI, and alleviate AKI *in vitro*.

The TK-SS31 linker in the ASMGS nanomotors was expected to be removed *via* ROS, thereby achieving on-demand SS31 release. H_2O_2, as an ROS, was used to assess the response of ASMGS nanomotors to ROS. HPLC was used to investigate the detachment of TK-SS31 and the release of SS31 from ASMGS nanomotors in the presence of 10 mM H_2O_2.[30] As shown in ESI Fig. S9,† SS31 was released in H_2O_2 (10 mM) over 72 h, whereas almost no release was observed in the absence of 10 mM H_2O_2. Thereafter, the amount of SS31 released from ASMGS nanomotors in the *in vitro* AKI model was measured, and the results are shown in ESI Fig. S10.† In addition, the ROS-stimulated release of SS31 from ASMGS nanomotors in HKC cells was assessed through CLSM. As shown in Fig. 4A, SS31 was colocalized with AF488-conjugated ASMGS nanomotors (green) in ROS-stimulated AKI model cells, whereas the colocalization of SS31 with AF488-conjugated ASMGS nanomo-

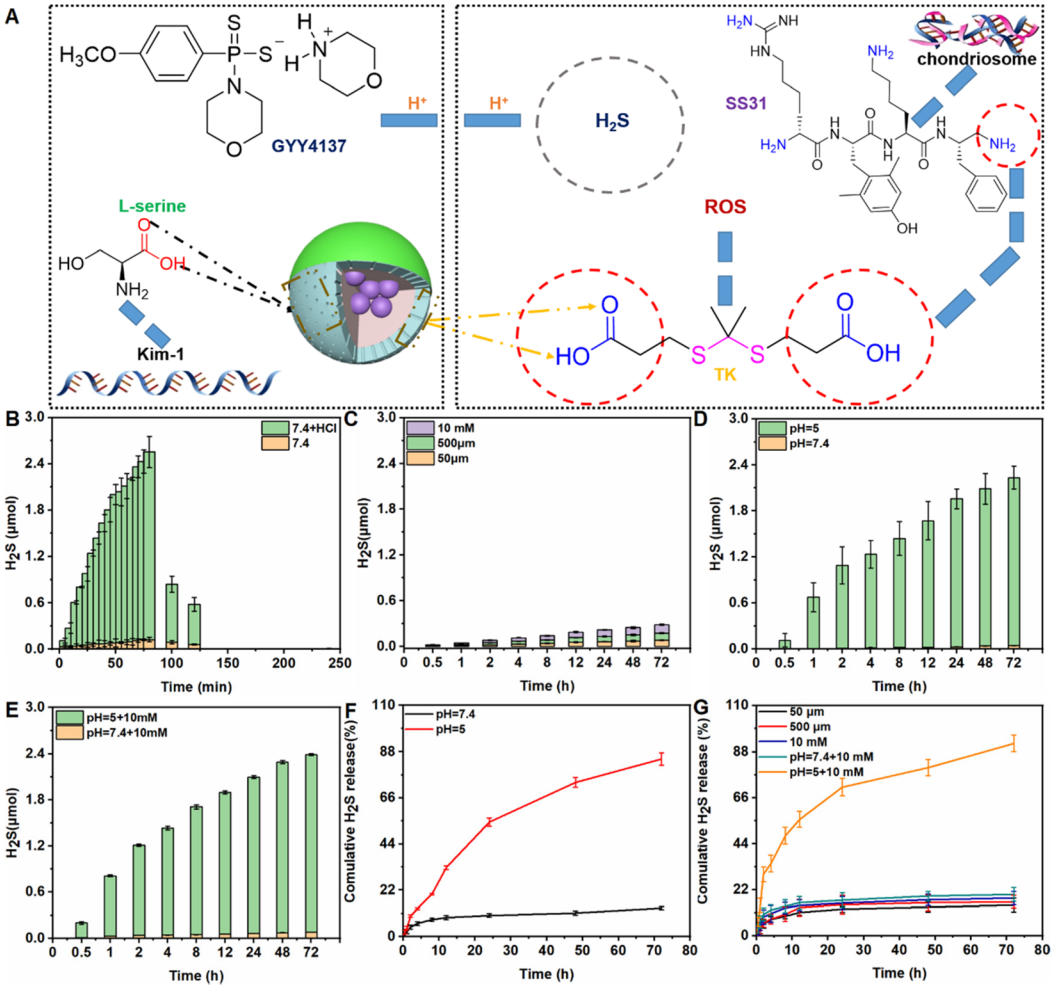

Fig. 1 Preparation and characterization of ASMGS nanomotors. (A) Preparation of ASMGS nanomotors. (B) Amount of H_2S released from GYY4137 in PBS (pH 7.4) + HCl and PBS (pH 7.4). (C) Amount of H_2S released from ASMGS nanomotors in a solution containing H_2O_2 (50 μm, 500 μm and 10 mM). (D) Amount of H_2S released from ASMGS nanomotors in PBS (pH 7.4) and PBS (pH 5.0). (E) Amount of H_2S released from ASMGS nanomotors in PBS (pH 7.4 + 10 mM H_2O_2) and PBS (pH 5.0 + 10 mM H_2O_2). (F) Release profiles of H_2S in PBS (pH 7.4) and PBS (pH 5.0). (G) release profiles of H_2S in the presence of 50 μm, 500 μm, 10 mM H_2O_2 and in an environment of pH 7.4 containing 10 mM H_2O_2 and an environment of pH 5.0 containing 10 mM H_2O_2 n = 3.

tors in normal HKC cells not treated with ROS was very weak. These results further corroborated that ASMGS nanomotors released SS31 in response to ROS in the mitochondria to exert a therapeutic effect on AKI *in vitro*. Furthermore, the mitochondrial membrane potential was assessed by CLSM, and the results are shown in Fig. 4B. The mitochondrial membrane potential was significantly decreased in AKI model cells compared to normal HKC cells, whereas ASMGS nanomotors obviously increased the mitochondrial membrane potential and ameliorated AKI *in vitro*.

Next, we further evaluated the change in ROS/H_2O_2 productions in the presence of ASMGS nanomotors in the *in vitro* AKI model. CLSM/kit was used to assess intracellular ROS/H_2O_2 generations after treatment with ASMGS nanomotors, and the results are shown in Fig. 5 and ESI Fig. S11.† After incubation with ASMGS nanomotors, ROS/H_2O_2 production significantly decreased *in vitro*, indicating that the nanocarrier improved the antioxidant capacity. Subsequently, the ROS removal efficiency was also observed after ASMGS nanomotor treatment (ESI Fig. S12†), showing that the nanoparticle could reduce the oxidative damage.

It is generally accepted that lysosomal-associated membrane protein 1 (LAMP1) expression is decreased in AKI.[37] We explored the effect of ASMGS nanomotors on the expression of LAMP1 in AKI *in vitro*. The expression of LAMP1 was significantly downregulated in AKI model cells compared to normal HKC cells, whereas ASMGS nanomotors increased the expression of LAMP1 (Fig. 6A). Taken together, these results indicated that ASMGS nanomotors improved lysosome function, including by restoring lysosome biogenesis and lysosome-mediated degradation, in AKI *in vitro*. Cysteinyl aspartate-specific proteinase-3 (caspase-3) is an apoptosis-related

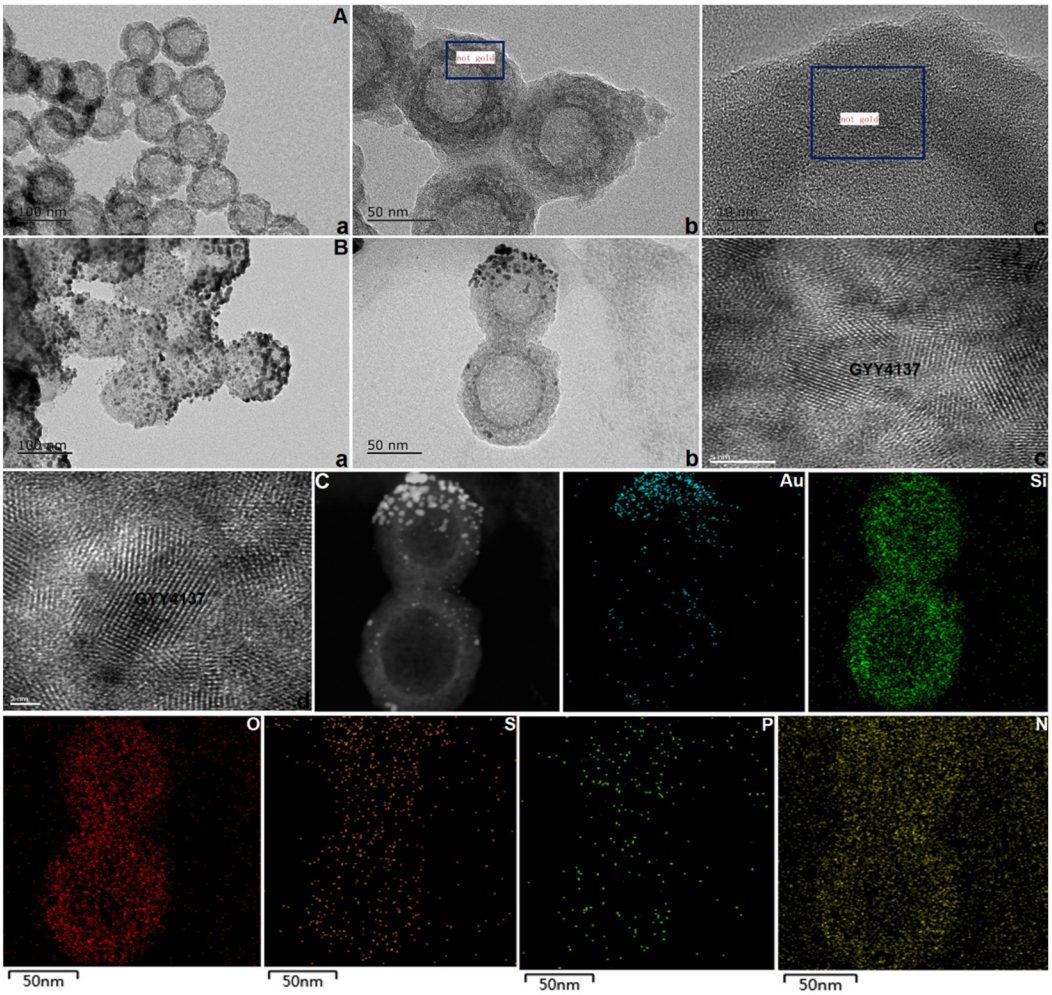

Fig. 2 Imaging analysis of ASMGS nanomotors. (A) TEM image of MSN (a, 100 nm; b, 50 nm; c, 10 nm). (B) TEM image of ASMGS nanomotors (a, 100 nm; b, 50 nm; c, 5 nm-GYY4137; d, 2 nm-GYY4137). (C) Mapping analysis of ASMGS nanomotors.

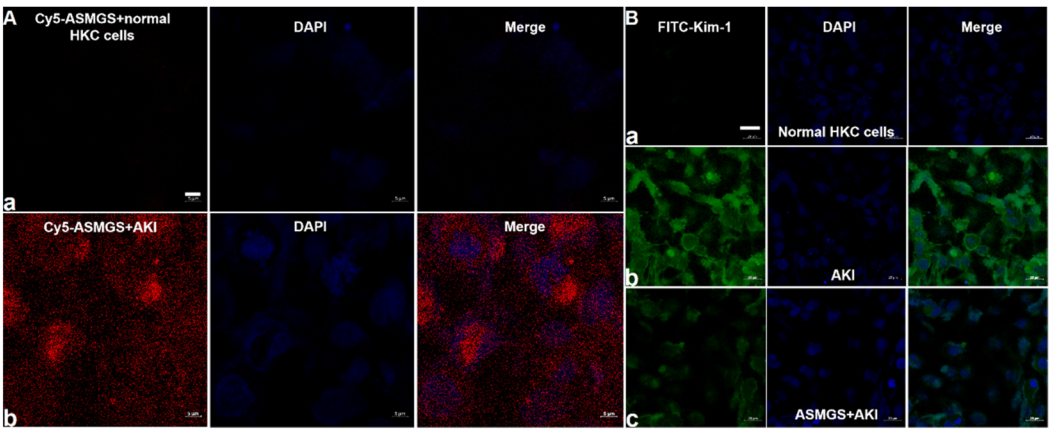

Fig. 3 Kim-1-associated endocytosis of ASMGS nanomotors in vitro. (A) CLSM images of Cy5-conjugated ASMGS nanomotors and DAPI in an *in vitro* AKI model (a, Cy5-ASMGS nanomotors + normal HKC cells; b, Cy5-ASMGS nanomotors + AKI model cells). Scale bar: 5 μm. (B) CLSM images of FITC-conjugated kim-1 and DAPI in an *in vitro* AKI model (a, normal HKC cells; b, AKI model cells; c, ASMGS nanomotors + AKI model cells). Scale bar: 20 μm.

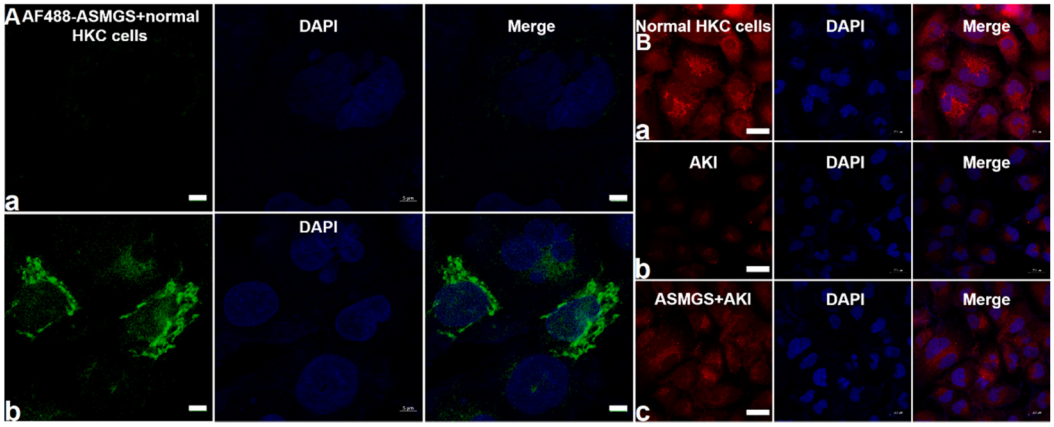

Fig. 4 ROS-triggered disruption of ASMGS nanomotors and mitochondrial transmembrane potential in AKI in vitro. (A) CLSM images or AF488-conjugated ASMGS nanomotors and DAPI in the mitochondria in the *in vivo* AKI model (a, ASMGS nanomotors + normal HKC cells; b, ASMGS nanomotors + AKI model cells). Scale bar: 5 μm. (B) Mitochondrial membrane potential was monitored by CLSM (a, normal HKC cells; b, AKI model cells; c, ASMGS nanomotors + AKI model cells). Scale bar: 20 μm.

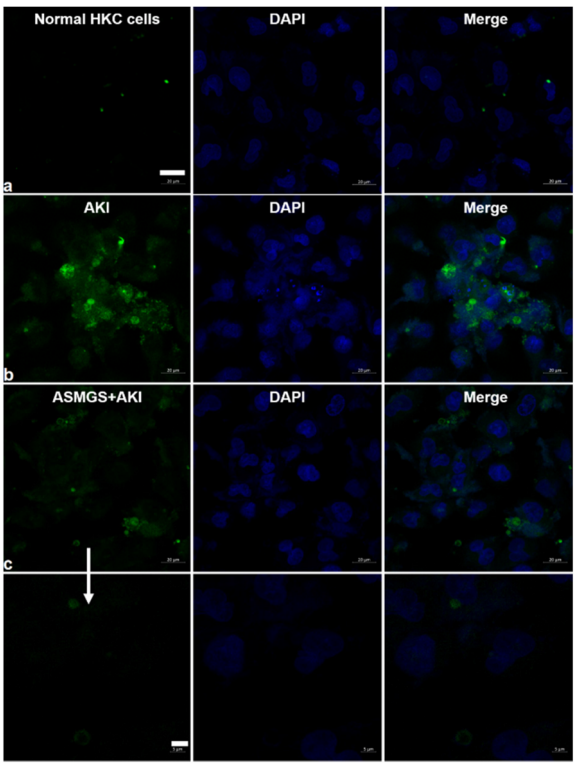

Fig. 5 Evaluation of ROS production in an in vitro AKI model. Intracellular ROS generation was assessed after treatment with ASMGS nanomotors *via* CLSM (a, normal HKC cells; b, AKI model cells; c, ASMGS nanomotors + AKI model cells). Scale bar: 20 and 5 μm.

protein.[38] Hence, we investigated the expression of caspase-3 in AKI *in vitro*. CLSM showed that the expression of caspase-3 was increased in AKI model cells compared to normal HKC cells and that ASMGS nanomotors obviously reduced the expression of Caspase-3 (Fig. 6B).

Previous research has confirmed that high-mobility group protein 1 (HMGB1) is involved in the inflammatory response during AKI.[39] The expression of HMGB1 in AKI model cells was higher than that in normal HKC cells. After administration of ASMGS nanomotors, the expression of HMGB1 was lower than that in AKI model cells not incubated with ASMGS nanomotors (Fig. 6C). These results indicated that ASMGS nanomotors could alleviate damage in the *in vitro* AKI model by inhibiting the release of HMGB1. Calreticulin (CRT) is an important contributor to renal dysfunction and fibrosis in kidney injury.[40,41] CRT expression was increased in the *in vitro* AKI model, and ASMGS nanomotors reduced CRT expression (Fig. 6D). In these *in vitro* studies, CRT was found to participate in kidney injury, and ASMGS nanomotors ameliorated AKI by downregulating CRT expression. In addition, the cytoskeleton observation was made and revealed in Fig. 7, and ASMGS evidently ameliorated cytoskeleton damnification. These results indicated that ASMGS could alleviate cell trauma in AKI *in vitro*.

Estimation of *in vitro* cell pyroptosis

Pyroptosis, a type of inflammatory cell death, is involved in AKI.[42] In AKI, cell pyroptosis is activated by GSDMD, inflammatory caspase-11 and the release of IL-18 and results in cell membrane disruption, pore formation, cell swelling, and the subsequent release of inflammatory factors.[42] Here, HKC cells were used to evaluate the role of GSDMD in AKI *in vitro*. We first confirmed that GSDMD expression was increased in AKI *in vitro* (Fig. 8A). After administration of ASMGS nanomotors, GSDMD expression was obviously decreased. As expected, caspase-11 and IL-18 expression was obviously decreased after ASMGS nanomotor treatment (Fig. 8B and C). Furthermore, cell pyroptosis in ASMGS nanomotor-treated cells compared with AKI model cells was assessed by TEM (Fig. 8D). All these results indicated that GSDMD-associated cell pyroptosis further exacerbates the inflammatory response and that ASMGS nanomotors could ameliorate cell pyroptosis.

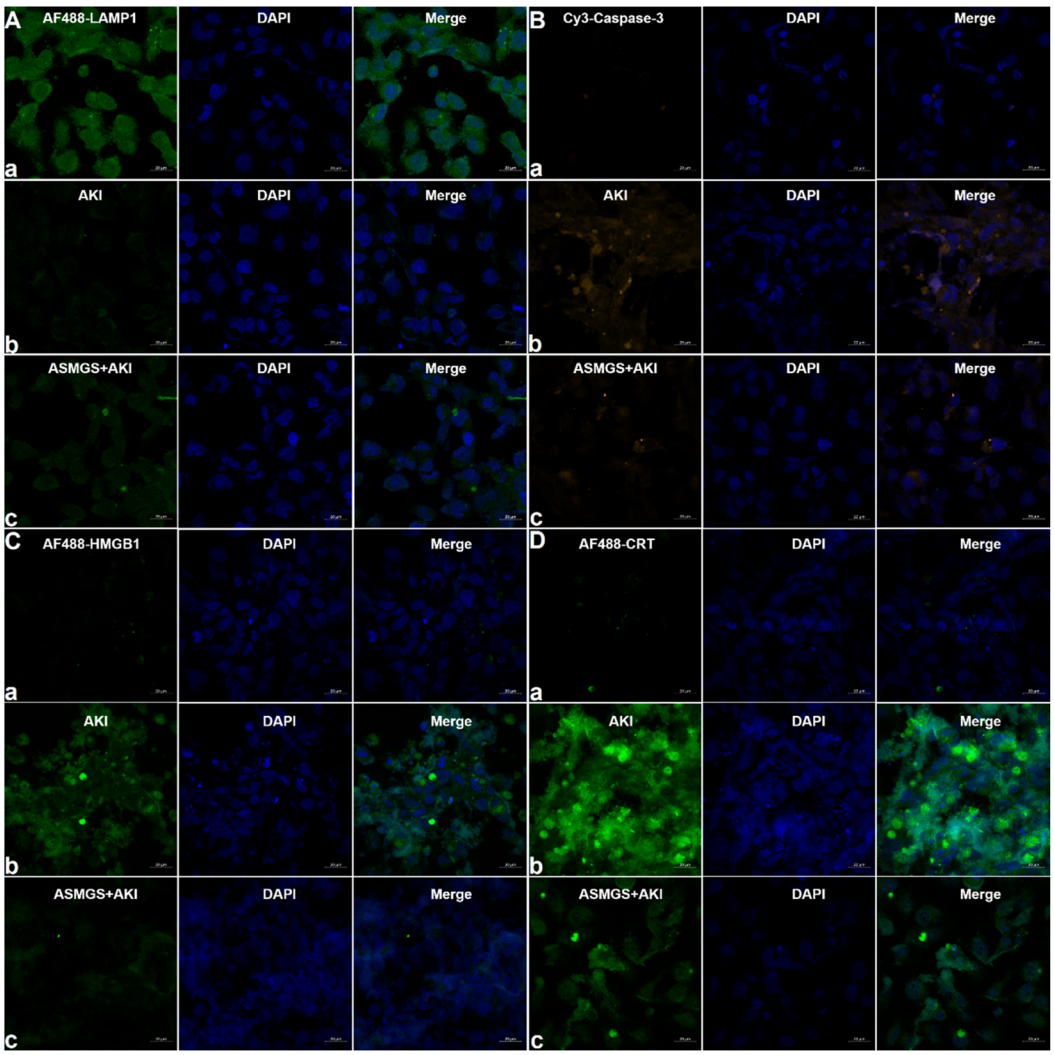

Fig. 6 LAMP1, caspase-3, HMGB1 and CRT expression in the in vitro AKI model. (A) CLSM images of AF488-conjugated LAMP1 and DAPI in the *in vitro* AKI model (a, normal HKC cells; b, AKI model cells; c, ASMGS nanomotors + AKI model cells). Scale bar: 20 μm. (B) CLSM images of Cy3-conjugated caspase-3 and DAPI in the *in vitro* AKI model (a, normal HKC cells; b, AKI model cells; c, ASMGS nanomotors + AKI model cells). Scale bar: 20 μm. (C) CLSM images of AF488-conjugated HMGB1 and DAPI in the *in vitro* AKI model (a, normal HKC cells; b, AKI model cells; c, ASMGS nanomotors + AKI model cells). Scale bar: 20 μm. (D) CLSM images of AF488-conjugated CRT and DAPI in the *in vitro* AKI model (a, normal HKC cells; b, AKI model cells; c, ASMGS nanomotors + AKI model cells). Scale bar: 20 μm.

Autonomous motion of nanomotors

After confirming that the nanomotors were successfully synthesized, we next attempted to assess the pH/ROS-induced motion of ASMGS nanomotors in PBS at different pH values, in a H_2O_2-containing solution and in a cell culture medium. An inverted fluorescence microscope equipped with a charge-coupled device (CCD) camera was used to record the movement of the nanomotors in real time for 10 s to create a video of 10 frames per second. In an acidic environment containing ROS, the motion of ASMGS nanomotors was enhanced in all media (Fig. 9A and Videos S1–5†). The mean square displacement (MSD) was further determined by simultaneously recording the x and y coordinates of multiple particles (20 particles) based on nanoparticle tracking analysis. The MSD curves were fitted to calculate the average velocity of asymmetrical PSMGS nanomotors using the self-diffusiophoretic model.[43] After laser irradiation, the MSD (Fig. 9B–D; ESI Fig. S13A–E†) and velocity values (Fig. 9E–G; ESI Fig. S13F–J†) of the pH/ROS-activated nanomotors indicated that they displayed directional and autonomous movements. The asymmetrical PSMGS nanomotors moved downward from the opening at a velocity of up to 4.05 μm s^{-1} in pH 5.0 PBS, at a velocity of up to 2.78 μm s^{-1} in 10 mM H_2O_2 PBS, at a velocity of up to 4.62 μm s^{-1} in pH 5.0 PBS + 10 mM H_2O_2 and at a velocity of up to 4.21 μm s^{-1} in pH 5.0 cell culture medium + 10 mM H_2O_2. Both the MSD and the velocity were increased, probably because more H_2S was released from the asymmetrical PSMGS nanomotors due to the acidic/ROS-containing environment. However, near-Brownian motion was observed, and the MSD curve had a shape (linear)

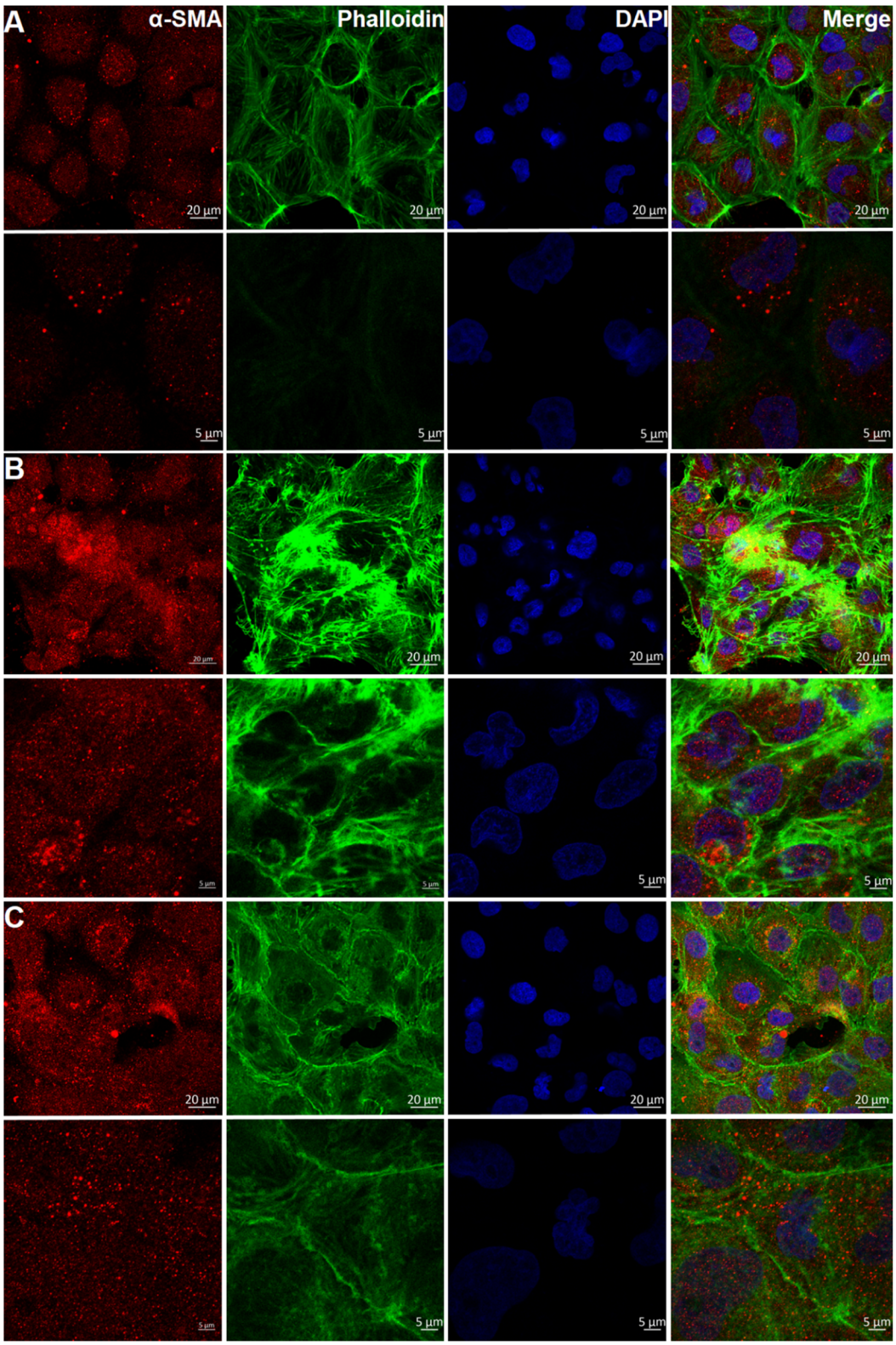

Fig. 7 Cytoskeleton observation in the in vitro AKI model. (A) Normal HKC cells. (B) AKI model cells. (C) ASMGS nanomotors + AKI model cells. (α-SMA: α-smooth muscle actin.) Scale bar: 20 and 5 μm.

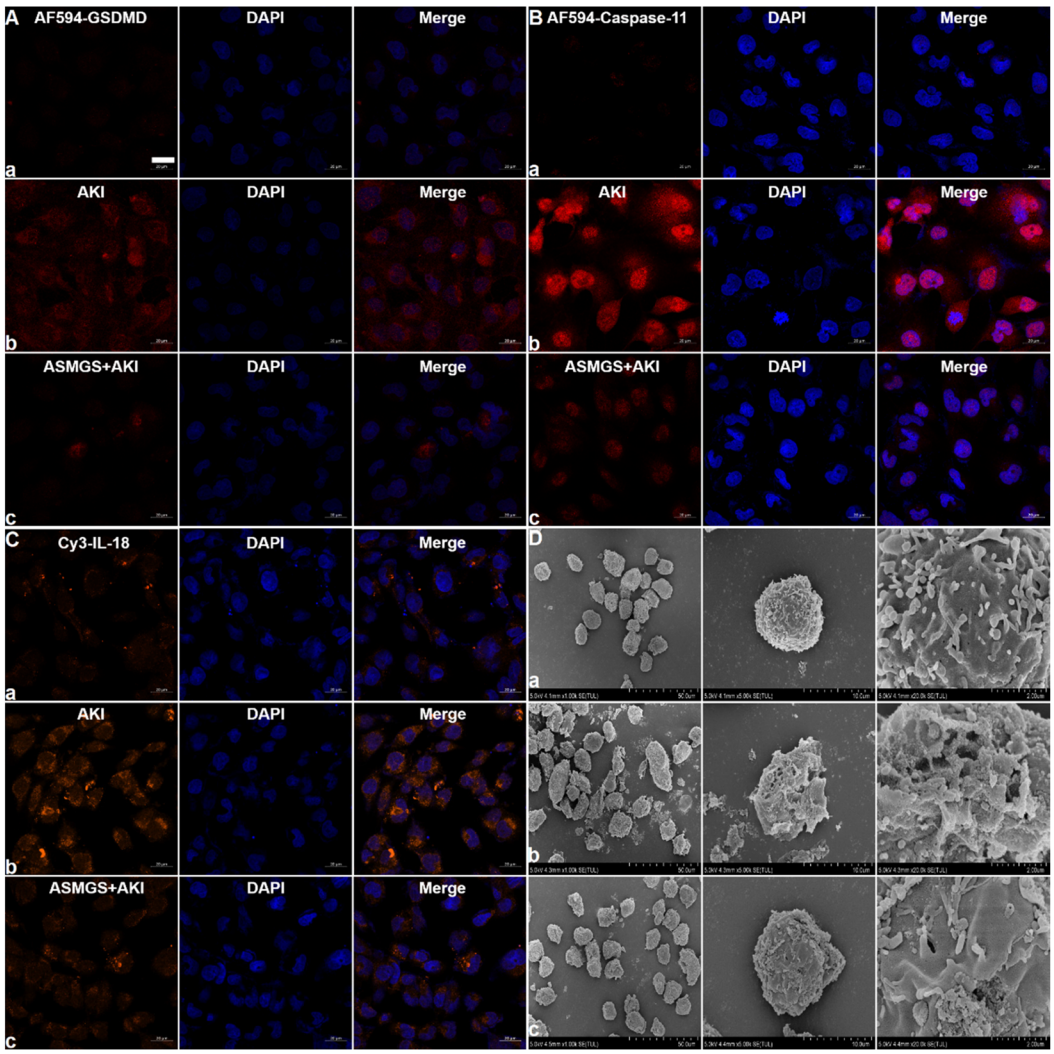

Fig. 8 Cell pyroptosis in the in vitro AKI model. (A) CLSM images of AF594-conjugated GSDMD and DAPI in AKI model cells incubated with ASMGS nanomotors (a, normal HKC cells; b, AKI model cells; c, ASMGS nanomotors). Scale bar: 20 μm. (B) CLSM images of AF594-conjugated caspase-11 and DAPI in AKI model cells incubated with ASMGS nanomotors (a, normal HKC cells; b, AKI model cells; c, ASMGS nanomotors). Scale bar: 20 μm. (C) CLSM images of AF488-conjugated IL-18 and DAPI in AKI model cells incubated with asymmetrical PSMGS nanomotors (a, normal HKC cells; b, AKI model cells; c, ASMGS nanomotors). Scale bar: 20 μm. (D) TEM images of pyroptosis in AKI model cells incubated with asymmetrical PSMGS nanomotors (a, normal HKC cells; b, AKI model cells; c, ASMGS nanomotors). Scale bars: 50 μm, 10 μm and 2 μm.

and size indicative of Brownian motion in the absence of an acidic/ROS-containing environment (Fig. 9B–D; ESI Fig. S13A–E†). Representative diffusion coefficients and tracking trajectories of asymmetrical PSMGS nanomotors in the presence and absence of an acidic/ROS-containing environment are presented in ESI Fig. S14 and 15,† respectively. The diffusion coefficients of the nanomotors were 0.18 ± 0.11 $\mu m^2\ s^{-1}$, 0.18 ± 0.16 $\mu m^2\ s^{-1}$ and 0.17 ± 0.19 $\mu m^2\ s^{-1}$ in PBS and cell culture media in the absence of an acidic/ROS-containing environment but were increased to 1.21 ± 0.15 $\mu m^2\ s^{-1}$, 1.02 ± 0.27 $\mu m^2\ s^{-1}$, 1.79 ± 0.28 $\mu m^2\ s^{-1}$, and 1.38 ± 0.27 $\mu m^2\ s^{-1}$ in pH 5.0 PBS, PBS containing 10 mM H_2O_2, pH 5.0 PBS containing 10 mM H_2O_2, and pH 5.0 cell culture medium containing 10 mM H_2O_2, respectively, indicating the occurrence of active self-propulsion.

In vivo targeting ability and biomineralization of ASMGS nanomotors

Having confirmed the therapeutic potential of our nanomotors *in vitro*, the biocompatibility and *in vivo* performance of ASMGS nanomotors were further assessed *in vivo* by fluorescence imaging. First of all, we observed the distribution of the nanoparticles in the kidney tissue by Bio-TEM (ESI Fig. S16†). Soon afterwards, as expected, the relative fluorescence intensity of ASMGS nanomotors in the damaged kidney was evidently enhanced (Fig. 10A). These results indicated that our nanomotor selectively targeted sites of kidney damage and that analysis of nanomotor accumulation in the damaged kidney through *in vivo* fluorescence imaging could be used as a noninvasive method for monitoring their targeting ability. Thereafter, the nanomotors

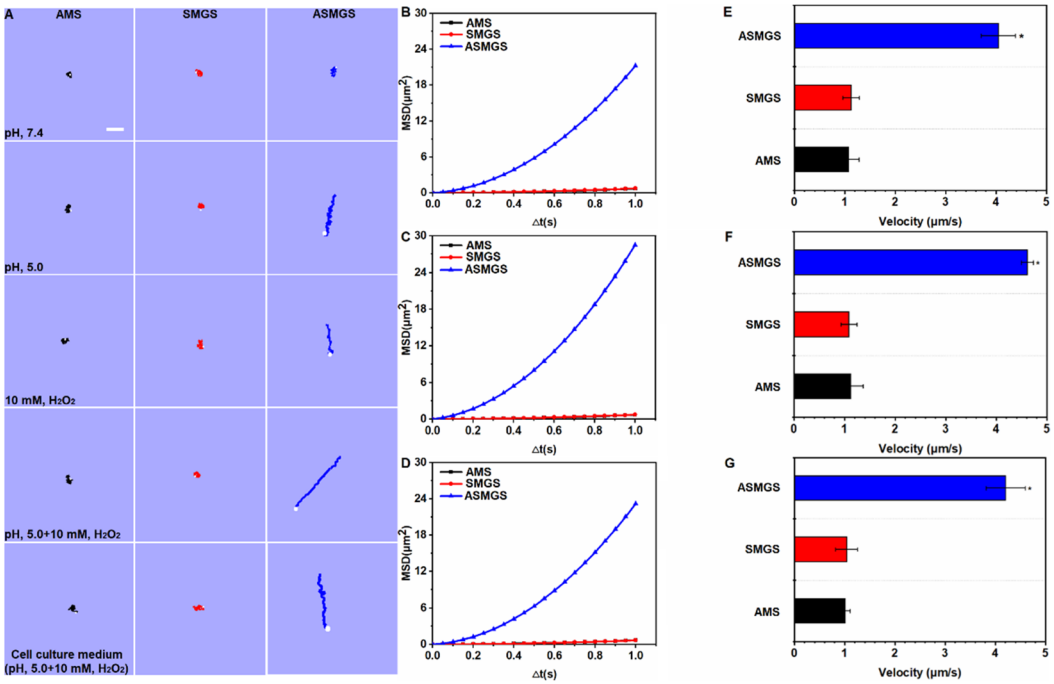

Fig. 9 Motion of nanomotors. (A) Time-lapse images of ASMGS nanomotors in different media. The MSD of ASMGS nanomotors in pH 5.0 PBS (B), pH 5.0 PBS containing 10 mM H_2O_2 (C) and pH 5.0 cell culture medium containing 5.0 + 10 mM H_2O_2 (D). The directional motion was fitted to the equation $(4D)\Delta t + (V^2)(\Delta t^2)$, and the Brownian motion was fitted to the equation $(4D)\Delta t$. The velocity of ASMGS nanomotors in pH 5.0 PBS (E), pH 5.0 PBS containing 10 mM H_2O_2 (F) and pH 5.0 cell culture medium containing 10 mM H_2O_2 (G). AMS, Au@MSN@S; SMGS, SS31-TK-MSN/GYY4137@S; ASMGS, Au@SS31-TK-MSN/GYY4137@S (20 particles).

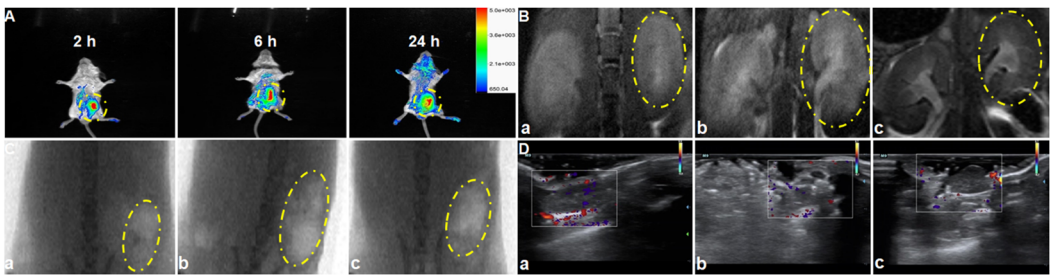

Fig. 10 *In vivo* biodistribution and observation of ASMGS nanomotors. (A) *In vivo* distribution of FITC-conjugated ASMGS nanomotors at different time points. (B) T_2 MR and X-ray (C) images after intravenous administration. (D) Brightness-mode ultrasound images of renal blood vessels after intravenous administration (a, control; b, AKI model; c, ASMGS nanomotors).

were imaged using an MR/X-ray scanner *in vivo*. In the AKI model, ASMGS nanomotors alleviated renal injury (Fig. 10B and C). Moreover, the change in renal blood flow after ASMGS nanomotor treatment was monitored using an MR/brightness-mode ultrasound scanner *in vivo*. More significant blood flow recovery was observed in the AKI model after ASMGS nanomotor treatment (Fig. 10D and ESI Fig. S17; Video S6†). This recovery of blood flow could be beneficial for alleviating AKI *in vivo*, and MR/brightness-mode ultrasound imaging could be used to assess the efficacy of treatment.

Pharmacological effect of ASMGS *in vivo*

After assessing the *in vivo* targeting ability and biomineralization of ASMGS, the serum H_2S and tissue SS31 contents were measured, and the results are shown in ESI Fig. S18 and 19.† Subsequently, the therapeutic effect of the ASMGS nanomotors in an AKI mouse model was analyzed. Fig. 11 shows the details of the treatment protocol. AKI model mice were injected intravenously with ASMGS nanomotors at a dose of 5 mg kg^{-1}. At 48 h after reperfusion, we dissected the kidney, liver, heart, and lung tissues and assessed the therapeutic effect. As shown in Fig. 11A and ESI Fig. S20–24,† the images and the levels of BUN, Scr, H_2O_2, SOD, MDA, TNF-α and IL-6 showed that AKI was obviously ameliorated in mice that received ASMGS nanomotors. Thus, the nanomotors exerted a better therapeutic effect than other treatments.

Then, immunohistochemical analysis of renal tissue sections was performed, and the results revealed that, compared

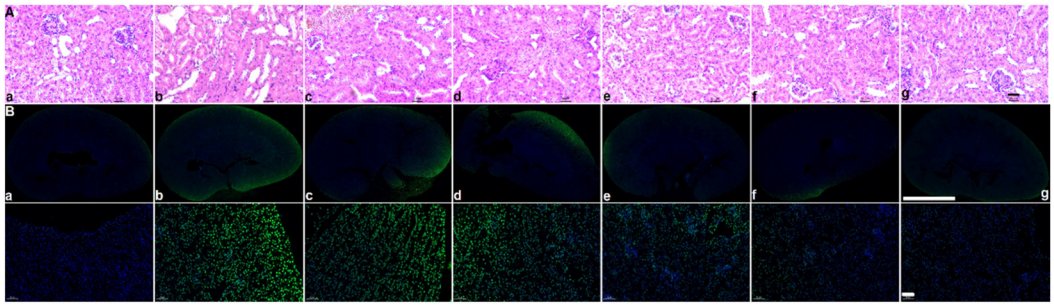

Fig. 11 *In vivo* HE and TUNEL staining. (A) HE staining of different tissues after different treatments (a, control; b, AKI model; c, SS31; d, GYY4137; e, SS31 + GYY4137; f, SMGS; g, ASMGS nanomotors). Scale bar: 50 μm. (B) TUNEL staining of different tissues after different treatments (a, control; b, AKI model; c, SS31; d, GYY4137; e, SS31 + GYY4137; f, SMGS; g, ASMGS nanomotors). Scale bars: 2000 μm and 50 μm.

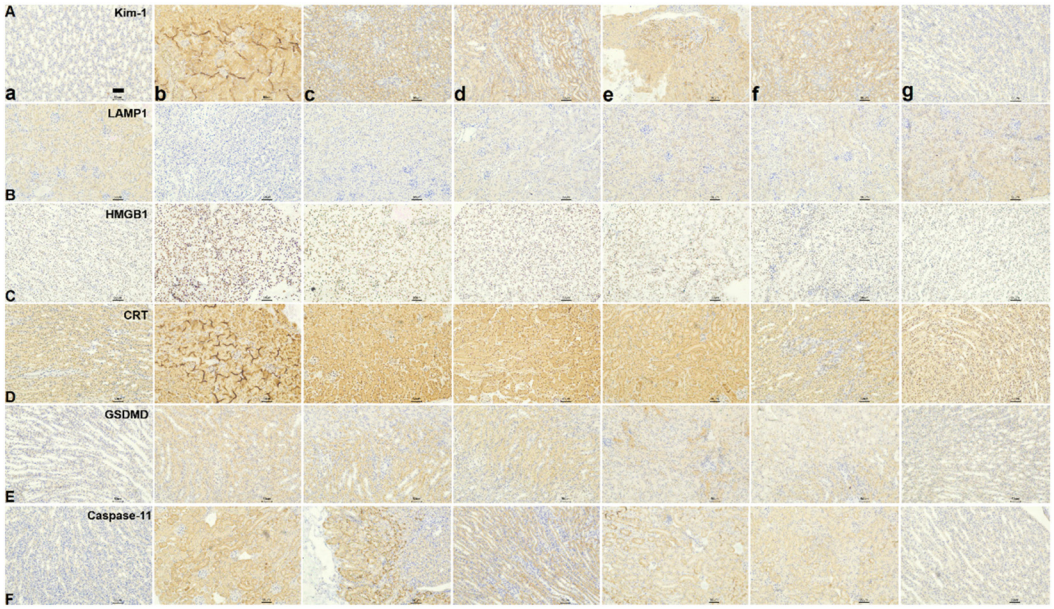

Fig. 12 *In vivo* immunohistochemical analysis. Kim-1 (A), LAMP1 (B), HMGB1 (C), CRT (D), GSDMD (E), and Caspase-11 (F), expressions in renal tissues after different treatments (a, control; b, AKI model; c, SS31; d, GYY4137; e, SS31 + GYY4137; f, SMGS; g, ASMGS nanomotors). Scale bar: 50 μm.

with control treatment, ASMGS nanomotor treatment resulted in less cell death. In addition, TUNEL staining in renal tissues further showed that apoptosis was effectively inhibited in the kidney after ASMGS nanomotor treatment (Fig. 11B). Subsequently, kim-1, LAMP1, HMGB1 and CRT expression was analyzed by immunochemistry (Fig. 12B–E). The results indicated that ASMGS nanomotor treatment could increase LAMP1 expression and decrease kim-1, HMGB1, and CRT expression, showing that the ASMGS nanomotors obviously relieved AKI. Next, GSDMD/Caspase-11 expressions were assessed, and it was found that ASMGS nanomotor treatment obviously decreased GSDMD/Caspase-11 expressions (Fig. 12F). In addition, urine IL-18 level was observed and ASMGS nanomotor significantly reduced IL-18 content (ESI Fig. S25†). These results indicated that the ASMGS nanomotors could inhibit cell pyroptosis to relieve AKI and reduce Renal function worsens.[44] Overall, these *in vivo* studies proved that ASMGS nanomotors are an excellent candidate for treating AKI with minimal biological side effects.

Discussion

In summary, we reported the synthesis of pH/ROS-sensitive ASMGS nanomotors and their ability to release H_2S/SS31 in an acidic/ROS-containing environment. Oxidative stress results from endogenous ROS in AKI, and the ASMGS nanomotors could release SS31 to inhibit oxidative stress injury in AKI models. Furthermore, the ASMGS nanomotors could release H_2S to alleviate AKI, implying that H_2S and SS31 had a synergistic therapeutic effect. In addition, this H_2S-mediated nanomotor strategy shows the advantages of precision therapies

over conventional treatments for AKI. This study provides novel insights into the potential value of nanomotors for the treatment of AKI.

Data availability

All data needed to assess the results in the article are present in the article and/or the ESI.† Additional data related to the article could be requested from the authors.

Author contributions

F. T., G. W. and Q. M. conceived and designed the experiments. F. T., L. L. and J. L. performed all experiments, analyzed the data and drafted the manuscript. All authors discussed the results and contributed to the final form of the manuscript.

Conflicts of interest

The authors declared no competing interests.

Acknowledgements

This work was supported by the China Postdoctoral Science Foundation (Grant No. 2021M692698), Shandong Province Nature Fund (Grant No. ZR2022ME168) and Funds for scientific research start-up of Binzhou Medical University.

References

1 R. Alobaidi, R. K. Basu, S. L. Goldstein, *et al.*, Sepsis-associated acute kidney injury, *Semin. Nephrol.*, 2015, **35**, 2–11.
2 J. L. Xue, F. Daniels, R. A. Star, *et al.*, Collins, Incidence and mortality of acute renal failure in Medicare beneficiaries, 1992 to 2001, *J. Am. Soc. Nephrol.*, 2006, **17**, 1135–1142.
3 R. Bellomo, J. A. Kellum and S. M. Bagshaw, Normotensive ischemic acute renal failure, *N. Engl. J. Med.*, 2007, **357**, 2205.
4 S. S. Waikar, G. C. Curhan, R. Wald, *et al.*, Declining mortality in patients with acute renal failure, 1988 to 2002, *J. Am. Soc. Nephrol.*, 2006, **17**, 1143.
5 L. S. Chawla, P. W. Eggers, R. A. Star, *et al.*, Acute kidney injury and chronic kidney disease asinterconnected syndromes, *N. Engl. J. Med.*, 2014, **371**, 58–66.
6 R. Bellomo, J. A. Kellum, C. Ronco, *et al.*, Acute kidney injury in sepsis, *Intensive Care Med.*, 2017, **3**, 1–13.
7 R. Wald, E. Mcarthur, N. K. J. Adhikari, *et al.*, Changing incidence and outcomes following dialysis-requiring acute kidney injury among critically Ill adults: apopulation-based cohort study, *Am. J. Kidney Dis.*, 2015, **65**, 870–877.
8 E. A. J. Hoste, J. A. Kellum, N. M. Selby, *et al.*, Global epidemiology and outcomes of acute kidney injury, *Nat. Rev. Nephrol.*, 2018, **14**, 607–625.
9 A. Khwaja, KDIGO clinical practice guidelines for acute kidney injury, *Nephron Clin. Pract.*, 2012, **120**, C179–C184.
10 Q. Chen, A. K. S. Camara, D. F. Stowe, *et al.*, Modulation of electron transport protects cardiac mitochondria and decreases myocardial injury during ischemia and reperfusion, *Am. J. Physiol.: Cell Physiol.*, 2007, **292**, C137–C147.
11 D. Liu, F. Y. Jin, G. F. Shu, *et al.*, Enhanced efficiency of mitochondria-targeted peptide SS-31 for acute kidney injury by pH-responsive and AKI-kidney targeted nanopolyplexes, *Biomaterials*, 2019, **211**, 57–67.
12 S. J. Han and H. T. Lee, Mechanisms and therapeutic targets of ischemic acute kidney injury, *Kidney Res. Clin. Pract.*, 2019, **38**, 427–440.
13 S. Tanaka, T. Tanaka and M. Nangaku, Hypoxia as a key player in the AKI-to-CKD transition, *Am. J. Physiol.: Renal Physiol.*, 2014, **307**, F1187–F1195.
14 G. Barrera, Oxidative stress and lipid peroxidation products in cancer progression and therapy, *ISRN Oncol.*, 2012, **2012**, 137289.
15 J. L. Martin, A. V. Gruszczyk, T. E. Beach, *et al.*, Mitochondrial mechanisms and therapeutics in ischaemia reperfusion injury, *Pediatr. Nephrol.*, 2019, **34**, 1167–1174.
16 P. Pallepati and D. A. Averillbates, Mild thermotolerance induced at 40 °C protects HeLa cells against activation of death receptor-mediated apoptosis by hydrogen peroxide, *Free Radical Biol. Med.*, 2011, **50**, 667–679.
17 E. Y. Plotnikov, A. V. Kazachenko, M. Y. Vyssokikh, *et al.*, The role of mitochondria in oxidative and nitrosative stress during ischemia/reperfusion in the rat kidney, *Kidney Int.*, 2007, **72**, 1493–1502.
18 A. I. Fishman, B. Alexander, M. Eshghi, *et al.*, Nephrotoxin-induced renal cell injury involving biochemical alterations and its prevention with antioxidant, *J. Clin. Med. Res.*, 2012, **4**, 95–101.
19 X. Yao, Effect of zinc exposure on HNE and GLT-1 in spinal cord culture, *Neurotoxicology*, 2009, **30**, 121–126.
20 C. H. Park, T. Tanaka, E. J. Cho, *et al.*, Glycerol-induced renal damage improved by 7-O-galloyl-D-sedoheptulose treatment through attenuating oxidative stress, *Biol. Pharm. Bull.*, 2012, **35**, 34–41.
21 H. H. Szeto, S. Liu, Y. Soong, *et al.*, Mitochondria-targeted peptide accelerates ATP recovery and reduces ischemic kidney injury, *J. Am. Soc. Nephrol.*, 2011, **22**, 1041–1052.
22 K. Zhao, G. M. Zhao, D. Wu, *et al.*, Cell-permeable peptide antioxidants targeted to inner mitochondrial membrane inhibit mitochondrial Swelling, oxidative cell death, and reperfusion injury, *J. Biol. Chem.*, 2004, **33**, 34682.
23 H. H. Szeto, First-in-class cardiolipin-protective compound as a therapeutic agent to restore mitochondrial bioenergetics, *Br. J. Pharmacol.*, 2014, **171**, 2029–2050.
24 A. V. Birk, S. Liu, Y. Soong, *et al.*, The mitochondrial-targeted compound SS-31 re-energizes ischemic mitochondria

by interacting with cardiolipin, *J. Am. Soc. Nephrol.*, 2013, **24**, 1250–1261.

25 W. Y. Zhao, S. Han, L. Zhang, *et al.*, Mitochondria-targeted antioxidant peptide SS31 prevents hypoxia/reoxygenation-induced apoptosis by down-regulating p66Shc in renal tubular epithelial cells, *Cell. Physiol. Biochem.*, 2013, **32**, 591–600.

26 H. H. Szeto, First-in-class cardiolipin-protective compound as a therapeutic agent to restore mitochondrial bioenergetics, *Br. J. Pharmacol.*, 2014, **171**, 2029–2050.

27 S. F. Hashmp, M. Z. A. Sattar, H. Rathore, *et al*., A critical review on pharmacological significance of hydrogen sulfide (H_2S) on NF-κB concentration, ICAM-1 expression in renal ischemia reperfusion injury, *Acta Pol. Pharm.*, 2017, **74**, 747–752.

28 Y. Chen, S. Jin, X. Teng, *et al.*, Hydrogen sulfide attenuates LPS-induced acute kidney injury by inhibiting inflammation and oxidative stress, *Oxid. Med. Cell. Longevity*, 2018, **2018**, 6717212.

29 R. Raggio, W. Bonani, E. Callone, *et al.*, Silk fibroin porous scaffolds loaded with a slow-releasing hydrogen sulfide agent (GYY4137) for applications of tissue engineering, *ACS Biomater. Sci. Eng.*, 2018, **4**, 2956–2966.

30 D. Liu, G. F. Shu, F. Y. Jin, *et al.*, ROS-responsive chitosan-SS31 prodrug for AKI therapy via rapid distribution in the kidney and long-term retention in the renal tubule, *Sci. Adv.*, 2020, **6**, eabb7422.

31 F. G. Zha, T. W. Wang, M. Luo, *et al.*, Tubular micro/nanomotors: propulsion mechanisms, fabrication techniques and applications, *Micromachines*, 2018, **9**, 78.

32 B. E. de Ávila, P. Angsantikul, J. Li, *et al.*, Micromotor-enabled active drug delivery for in vivo treatment of stomach infection, *Nat. Commun.*, 2017, **8**, 272.

33 M. M. Wan, Q. Wang, X. Y. Li, *et al.*, Systematic research and evaluation models of nanomotors for cancer combined therapy, *Angew. Chem., Int. Ed.*, 2020, **59**, 14458–11446.

34 F. Tong, Y. C. Ye, B. Chen, *et al.*, Bone-targeting prodrug mesoporous silica-based nanoreactor with reactive oxygen species burst for enhanced chemotherapy, *ACS Appl. Mater. Interfaces*, 2020, **12**, 34630–34642.

35 G. J. Freeman, J. M. Casasnovas, D. T. Umetsu, *et al.*, TIM genes: A family of cell surface phosphatidylserine receptors that regulate innate, adaptive immunity, *Immunol. Rev.*, 2010, **235**, 172–189.

36 S. Matsuura, H. Katsumi, H. Suzuki, *et al.*, L-Serine-modified polyamidoamine dendrimer as a highly potent renal targeting drug carrier, *Proc. Natl. Acad. Sci. U. S. A.*, 2018, **115**, 10511–10516.

37 R. Li, X. Zhao, S. Zhang, *et al.*, RIP3 impedes transcription factor EB to suppress autophagic degradation in septic acute kidney injury, *Cell Death Dis.*, 2021, **12**, 593.

38 P. Wang, N. Li, X. Wang, *et al.*, RIG-I, a novel DAMPs sensor for myoglobin activates NF-κB/caspase-3 signaling in CS-AKI model, *Mil. Med. Res.*, 2021, **8**, 37.

39 Y Wang, H Zhang, Q Chen, *et al.*, TNF–α/HMGB1 inflammation signalling pathway regulates pyroptosis during liver failure and acute kidney injury, *Cell Proliferation*, 2020, **53**, e12829.

40 F. Aregger, D. E. Uehlinger, J. Witowski, *et al.*, Identification of IGFBP-7 by urinary proteomics as a novel prognostic marker in early acute kidney injury, *Kidney Int.*, 2014, **85**, 909–919.

41 A. Lu, M. A. Pallero, B. Y. Owusu, *et al.*, Murphy-Ullrich, Calreticulin is important for the development of renal fibrosis and dysfunction in diabetic nephropathy, *Matrix Biol. Plus*, 2020, **8**, 100034.

42 W. Xia, Y. Li, M. Wu, *et al.*, Gasdermin E deficiency attenuates acute kidney injury by inhibiting pyroptosis and inflammation, *Cell Death Dis.*, 2021, **12**, 139.

43 M. Wan, Z. Liu, T. Li, *et al.*, Zwitterion-based hydrogen sulfide nanomotors induce multiple acidosis in tumor cells by destroying tumor metabolic symbiosis, *Angew. Chem., Int. Ed.*, 2021, **60**, 16139–16148.

44 N. Miao, F. Yin, H. Xie, *et al.*, The cleavage of gasdermin D by caspase-11 promotes tubular epithelial cell pyroptosis and urinary IL-18 excretion in acute kidney injury, *Kidney Int.*, 2019, **96**, 1105–1120.

